ACS OMEGA

http://pubs.acs.org/journal/acsodf

Article

Newly Synthesized Three-Dimensional Boron-Rich Chalcogenides $B_{12}X$ (X = S and Se): Theoretical Characterization of the Physical Properties for Optoelectronic and Mechanical Applications

Md. Mukter Hossain,* Md. Ashraf Ali, Md. Mohi Uddin, Saleh Hasan Naqib,* and A. K. M. Azharul Islam*

Cite This: *ACS Omega* 2021, 6, 33899−33913

Read Online

ACCESS | Metrics & More | Article Recommendations

ABSTRACT: Boron-rich chalcogenides have been predicted to have excellent properties for optical and mechanical applications in recent times. In this regard, we report the electronic, optical, and mechanical properties of recently synthesized boron-rich chalcogenide compounds $B_{12}X$ (X = S and Se) using density functional theory for the first time. The effects of exchange and correlation functionals on these properties are also investigated. The consistency of the obtained crystal structure with the reported experimental results has been checked in terms of lattice parameters. The considered materials are mechanically stable, brittle, and elastically anisotropic. Furthermore, the elastic moduli and hardness parameters are calculated, which show that $B_{12}S$ can be treated as a prominent member of the hard materials family compared to $B_{12}Se$. The origin of differences in hardness is explained on the basis of density of states near the Fermi level. Reasonably good values of fracture toughness and the machinability index for $B_{12}X$ (X = S and Se) are reported. The melting point, T_m, for the $B_{12}S$ and $B_{12}Se$ compounds suggests that both solids are stable, at least up to 4208 and 3577 K, respectively. Indirect band gaps of $B_{12}S$ (2.27 eV) and $B_{12}Se$ (1.30 eV) are obtained using the HSE06 functional. The energy gaps using local density approximation (LDA) and generalized gradient approximation (GGA) are found to be significantly lower. The electrons of the $B_{12}Se$ compound show a lighter average effective mass than that of the $B_{12}S$ compound, which signifies a higher mobility of charge carriers in $B_{12}Se$. The optical properties such as the dielectric function, refractive index, absorption coefficient, reflectivity, and loss function are characterized using GGA-PBE and HSE06 methods and discussed in detail. These compounds possess bulk optical anisotropy, and excellent absorption coefficients in the visible-light region along with very low static values of reflectivity spectra (range of 7.42−14.0% using both functionals) are noted. Such useful features of the compounds under investigation show promise for applications in optoelectronic and mechanical sectors.

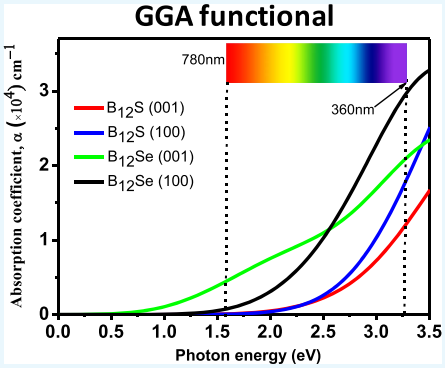

1. INTRODUCTION

Boron (B)-rich compounds having structural units of B_{12} closed cage clusters are novel systems attracting significant interest of the research community.[1−6] Many interesting physical properties such as high hardness, useful electronic properties, low mass density, a very high melting point, and excellent thermal stability and chemical inertness of B-rich compounds have gained extra attention of the materials science and engineering research community in view of the potential technical applications.[1,6] Among the B-rich compounds, the B-rich solids with icosahedral clusters[1,6,7] structurally derived from α-rhombohedral boron (α-rh boron) offer some industrial potential candidate materials similar to boron carbide, boron sub-oxide and boron sub-phosphide, $REB_{15.5}CN$, $REB_{22}C_2N$, and $REB_{28.5}C_4$ (RE = heavy rare-earth element, Y, and Sc). Recent discovery of B-rich compounds has received considerable research attention for the betterment of the physical properties in these days.[1−3,5,7−14] Very recently, Cherednichenko et al.[8] have synthesized 3D B-rich compounds $B_{12}S$ and $B_{12}Se$ using a chemical reaction process at a pressure of 6 GPa and a temperature of 2500 K. With the help of powder X-ray diffraction and Raman spectroscopy, it is found that the crystal structure belongs to rhombohedral symmetry with the space group $R\bar{3}m$ (no. 166). The stoichiometric ratio of the chalcogenides has been computed. Furthermore, only the bulk modulus of $B_{12}Se$ among all mechanical properties has been studied using the third-order Birch−Murnaghan equation

Received: September 17, 2021
Accepted: November 25, 2021
Published: December 3, 2021

Table 1. Optimized Crystallographic Lattice Parameters, *a* and *c* (All in Å), and the Unit Cell Volume *V* (Å^3) of Boron Sub-sulfide ($B_{12}S$) and Boron Sub-selenide ($B_{12}Se$) Compounds along with Literature Data

phase	*a*	*c*	*V*	occupancy (%)	functional	ref.
$B_{12}S$	5.8392	12.1115	357.6302	55	LDA-CAPZ	this work
	5.9118	12.3155	372.7574	55	GGA-PBE	this work
	5.8196	11.9653	364.76	55	exp.	8
	5.8966	12.1135		100		8
	5.80	11.90		50		31
	5.810	11.94		48.5		32
	5.8624	12.147		65		32
	5.8379	12.036		59.9		14
	5.8307	12.028		60.9		14
	5.8273	12.025		62		14
$B_{12}Se$	6.0237	12.1596	382.1013	52	LDA-CAPZ	this work
	6.0786	12.3713	395.8673	52	GGA-PBE	this work
	5.9385	11.9144	385.42	52	exp.	8
	6.0496	12.1603		100		8
	5.9041	11.947		46.9		5

of state so far.[7] In 2021, Solozhenko[15,16] measured the microhardness of 3D B-rich compounds $B_{12}S$ and $B_{12}Se$ experimentally using Vicker hardness (H_V) and Knoop hardness (H_K) methods and also studied the oxidation resistance by thermal analysis. The author reported that both chalcogenides belong to a family of hard compounds.

The structure of the B_{12} icosahedral boron network is also found in some other compounds similar to $B_{12}S$ and $B_{12}Se$. For instance, the chalcogenide compounds B_6S and B_6Se have already been synthesized by a chemical reaction process at high pressures.[1] A comprehensive theoretical study of the structural, electronic, mechanical, optical, and thermal properties of these two compounds has been reported recently, which demonstrated their potential for a variety of thermo-mechanical applications.[1,6] The boron-rich compounds $B_{12}C_3$,[9,10] $B_{12}O_2$,[10,11] and $B_{12}As_2$[2] were also reported as very hard compounds with good mechanical strength, superior mechanical stability, and the ability to function in harsh environments. Furthermore, Korozlu et al.[12] and Pan and Jia[13] have reported the mechanical properties and in particular the hardness values of some B-rich compounds using various models. They concluded that most of the B-rich chalcogenide compounds are usually prominent members of hard and superhard families. Since the structure of boron-rich B_{12} icosahedra supports the unusual physical and chemical properties, better knowledge especially related to the physical properties of $B_{12}S$ and $B_{12}Se$ could help design new application-oriented tasks.

However, many decisive properties of $B_{12}S$ and $B_{12}Se$ compounds like electronic (band structure, density of states, charge density, and Mulliken population analysis), optical (dielectric function, absorption coefficient, photoconductivity, reflectivity, loss function, and refractive index), and mechanical (elastic stiffness constant, polycrystalline moduli, hardness, fracture toughness, machinability index, melting point, etc.) are still unexplored. Understanding these properties is a matter of prime interest in order to disclose the full potential of the compounds of interest for possible device applications.

In the present contribution, the structural, electronic, mechanical, and optical properties of newly synthesized B-rich chalcogenide compounds $B_{12}X$ (X = S and Se) have been investigated meticulously with the help of the first-principles method based on density functional theory (DFT) for the first time. The obtained results confirmed that $B_{12}X$ (X = S and Se) are indirect band gap semiconductors that are likely to be hard materials and can also be used as an optical absorber in photovoltaic devices as well as optical waveguides. We have also carried out a comparative analysis of the physical properties of $B_{12}X$ (X = S and Se) with other similar B-rich compounds, where available.

2. THEORETICAL METHODOLOGIES

In the present report, we focus on the analysis and discussion of the structural, electronic, optical, and mechanical properties of newly synthesized B-rich chalcogenide compounds $B_{12}X$ (X = S and Se). To carry out these tasks, a first-principles approach based on state-of-the-art density functional theory (DFT) has been employed.[17,18] The high-throughput calculations are implemented in the CAmbridge Serial Total Energy Package (CASTEP) module.[19] The choice of the pseudopotential is quite important in view of optimization of the crystal structure and its electronic structure, especially of the semiconductor materials.[6,20,21] The exchange−correlation potentials are evaluated by using the functional form of Perdew−Burke−Ernzerhof (PBE) type within the generalized gradient approximation (GGA) and also of Ceperly and Alder−Perdew and Zunger (CA-PZ) type within the local density approximation (LDA).[18,22,23] The optimizations for both chalcogenide crystal structures are done by the Broyden−Fletcher−Goldfarb−Shanno (BFGS) method[24] using the following optimization input parameters: a plane wave basis set kinetic energy cutoff of 550 eV, a Monkhorst−Pack *k*-point mesh size[25] of 6×6×3, an energy convergence threshold of 5×10^{-6} eV/atom, a maximum force of 0.01 eV/Å, a maximum stress of 0.02 GPa, and a maximum atomic displacement of 5×10^{-4} Å. Very often, the band gap estimation of semiconductor materials using local functionals like LDA and GGA does not match with experimental results and underestimates the actual values. The electronic band gaps of both title compounds, therefore, are calculated as accurately as possible by using the nonlocal hybrid functional HSE06 (Heyd−Scuseria−Ernzerhof).[26−28] Elastic stiffness constants can be found by the "stress−strain" method supported by the CASTEP code.[29] The optical properties such as the real part of the dielectric function $[\varepsilon_1(\omega)]$, refractive index, absorption spectrum, loss function, reflectivity, and optical conductivity can be estimated following the Kramers−Kronig transformation relation from the

https://doi.org/10.1021/acsomega.1c05172
ACS Omega 2021, 6, 33899−33913

imaginary part of the dielectric function, $[\varepsilon_2(\omega)]$. The following equations are used to estimate the aforementioned optical constants where the symbols bear the usual significances:[19,29,30]

$$\varepsilon_2(\omega) = \frac{2e^2\pi}{\Omega\varepsilon_0}\sum_{k,v,c}|\psi_k^c|\boldsymbol{u}\cdot\boldsymbol{r}|\psi_k^v|^2\delta(E_k^c - E_k^v - E)$$

$$\varepsilon_1(\omega) = 1 + \frac{2}{\pi}P\int_0^\infty \frac{\omega'\varepsilon_2(\omega')\mathrm{d}\omega'}{(\omega'^2 - \omega^2)}$$

$$n(\omega) = \frac{1}{\sqrt{2}}[\sqrt{\{\varepsilon_1(\omega)\}^2 + \{\varepsilon_2(\omega)\}^2} + \varepsilon_1(\omega)]^{1/2}$$

$$\alpha(\omega) = \sqrt{2}\,\omega[\sqrt{\{\varepsilon_1(\omega)\}^2 + \{\varepsilon_2(\omega)\}^2} - \varepsilon_1(\omega)]^{1/2}$$

$$L(\omega) = \varepsilon_2(\omega)/[\{\varepsilon_1(\omega)\}^2 + \{\varepsilon_2(\omega)\}^2]$$

$$R(\omega) = \left|\frac{\sqrt{\varepsilon(\omega)} - 1}{\sqrt{\varepsilon(\omega)} + 1}\right|^2$$

3. RESULTS AND DISCUSSION

3.1. Structural Properties. The crystal structures of two B-rich chalcogenide compounds $B_{12}S$ and $B_{12}Se$ are isostructural to α-rhombohedral boron (α-B_{12}). The titled compounds contain 10 (ten) B_{12} icosahedra (a three-dimensional polyhedral rigid network) in the hexagonal unit cell in which eight icosahedral units are found at corner positions and the other two are placed on one of the main diagonals.[8] The crystallographic lattice parameters of both chalcogenides under study are presented in Table 1, along with previously reported data. The optimized crystal structure of $B_{12}S$ as a prototype structure is depicted in Figure 1. It is obvious that the lattice

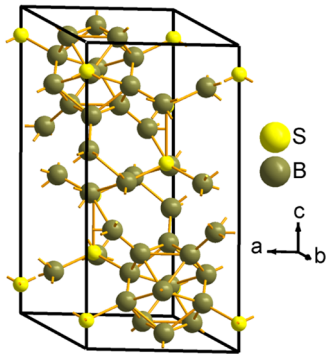

Figure 1. Schematic crystal structure of the $B_{12}S$ chalcogenide compound belonging to the rhombohedral symmetry with the space group $R\bar{3}m$ (no. 166). Two icosahedral units are found on one of the main diagonals. The $B_{12}Se$ chalcogenide compound is completely isostructural to $B_{12}S$ and is not shown here.

constants and bond lengths of both studied compounds could be different due to the variation of the electronegativity and atomic number of the 6c site element (S/Se). In Table 1, there have been some minor variations of both lattice constants (a and c) in the literature data due to the variation of S/Se occupancy in the unit cell. It was reported that the level of occupancy of S atoms at the 6c site is 55% and that of Se at the 6c site is 52%, while all the boron atoms form B_{12} icosahedra having occupancies at 18h sites that are found to be 100%. These results reveal an excellent final reliability factor of the Rietveld refinement analysis as well as of the energy-dispersive X-ray spectroscopy data.[8] However, the calculated lattice parameters using the LDA-CAPZ functional show fair agreement with other literature data compared to those obtained via GGA-PBE.

3.2. Electronic Properties, Charge Density, and Mulliken Population. The electronic band structures (EBS) along high-symmetry directions of $B_{12}S$ and $B_{12}Se$ are illustrated in Figure 2. The Fermi level (E_F) is set to 0 eV. In many semiconducting materials, band gap estimation using local functionals results in inaccurate values along with inappropriate positions of the valence band (VB) and the conduction band (CB), which lead the theoretical study far-off from the experimental results. The error might emanate from strong Coulomb correlations of the material. In most of the cases, the use of nonlocal functionals could be a fair solution to the aforementioned problem.[27,28] In order to provide an accurate prediction of the EBS as well as the band gap, we have used both local functionals (LDA and GGA) and a nonlocal functional (HSE06) to model the exchange−correlation potential. At present, due to the lack of literature data, comparison of EBS results with any experimental and/or theoretical ones is not possible. All the results presented in this section will require experimental validation. However, as depicted from Figure 2, the bottom of the CB is at a fixed position at the A point of the Brillouin zone for both the compounds, while the top of the VB is located at different places: the M point and the Γ point for $B_{12}S$ and $B_{12}Se$, respectively. This implies that both the chalcogenides should be indirect band gap semiconductors.

The value of the indirect band gap is very sensitive to the exchange and correlation functional as shown in Figure 2. The values of indirect band gaps (in eV) for $B_{12}S$ ($B_{12}Se$) compounds using LDA, GGA, and HSE06 functionals are found to be 1.287 (0.0), 1.245 (0.093), and 2.271 (1.300), while those of minimum direct band gaps at the M point (Γ point) are 1.985 (1.495), 2.161 (1.564), and 2.746 (2.344), respectively. The band morphology was significantly affected by the chalcogenide element (X element). For instance, due to the replacement of the S element with Se in the $B_{12}S$ compound, all valence and conduction bands (in case of use of both local and nonlocal functionals) are shifted toward the E_F with minor variation in the shape of the bands. Similar results were also reported in the B-rich chalcogenide B_6X (X = S and Se) compounds.[6] Furthermore, the top of the VB was shifted from the M point to the Γ point when the S element was substituted by the Se atom to form the compound $B_{12}Se$. It is also seen that the bands along H−K and H−L directions for both compounds are much less dispersive than in any other direction. Furthermore, the bottom of the CB and the top of the VB based on the band morphology inspection inspire us to calculate the effective mass, which can predict the charge transport behaviors. The effective masses of electrons (m_e^*) and holes (m_h^*) for the CB and the VB have been calculated, respectively, using the following equation:[33]

$$m^* = \frac{\hbar^2}{\left(\frac{d^2\varepsilon(k)}{dk^2}\right)}$$

https://doi.org/10.1021/acsomega.1c05172
ACS Omega 2021, 6, 33899−33913

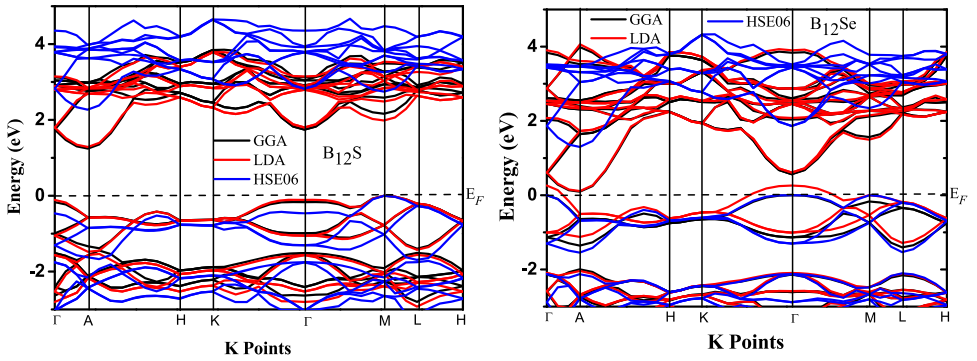

Figure 2. Electronic band structures of boron-rich chalcogenide compounds $B_{12}S$ and $B_{12}Se$ along the high-symmetry directions using local (GGA and LDA) and nonlocal (HSE06) functionals. The black dashed horizontal lines denote the Fermi level (E_F), which are set to 0 eV.

where k is the wave vector, $\varepsilon(k)$ is the eigenvalue of the energy band at the wave vector, k, and $\hbar$ is the reduced Planck constant. It is obvious from the equation that the value of m^* has an inverse relationship with the curvature of the electronic band dispersions. The calculated carrier effective masses (m_e^*m and m_h^*m), average effective masses (m_{dc} and m_{dv}) in the CB and VB, respectively, using HSE06 functionals, and band gaps (in eV) for boron sub-sulfide ($B_{12}S$) and boron sub-selenide ($B_{12}Se$) compounds are displayed in Table 2. The average effective masses m_{dc} and m_{dv} at the CB and the VB, respectively, are calculated using standard formulae that can be found elsewhere.[33,34]

Table 2. Carrier Effective Masses (m_e^* and m_h^*), Average Effective Masses (m_{dc} and m_{dv}) in the Conduction and Valence Bands, Respectively, Using HSE06 Functionals, and Band Gaps (eV) for Boron Sub-sulfide ($B_{12}S$) and Boron Sub-selenide ($B_{12}Se$) Compounds

parameters/approach	$B_{12}S$	$B_{12}Se$	ref.
$m_e^*(m_0)$	0.98 A(A→Γ)	0.96 A(A→Γ)	this
	1.07 A(A→H)	0.59 A(A→H)	
$m_{dc}(m_0)$	1.02	0.75	this
$m_h^*(m_0)$	1.85 M(M→Γ)	3.50 Γ(Γ→M)	this
	2.04 M(M→L)	3.24 Γ(Γ→K)	
$m_{dv}(m_0)$	1.94	3.37	this
band gap (eV) (LDA-CAPZ)	1.287	0.000	this
band gap (eV) (GGA-PBE)	1.245	0.093	this
band gap (eV) (HSE06)	2.271	1.300	this

The calculated effective masses of electrons (m_e^*) at the A point along (A→Γ) and (A→H) directions in the CB for both compounds are different due to the difference in curvatures of the bands. Similar results are also found for holes in the VB as shown in Table 2. In the $B_{12}Se$ compound, the m_{dc} has a light effective mass compared to that of the $B_{12}S$ compound, which originates from dispersive p orbitals of the B element in the former. In contrast to m_{dc}, the m_{dv} with a value of $3.37m_0$ at the Γ point for the $B_{12}Se$ compound is much heavier than $1.94m_0$ at the M point for the $B_{12}S$ compound. Here, m_0 is the bare electron mass. This indicates that a less dispersive curvature (almost flat band) is formed at the Γ point in comparison to that at the M point. Note here that the top of the VB was shifted from the M to the Γ point with the replacement of the S atom with the Se element. It is known that the effective mass can predict the carrier mobility as well as the carrier concentration of a semiconductor material and is often used to predict the electrical conductivity of solids. A low value of m_{dc} for $B_{12}Se$ should indicate a high carrier mobility as well as electrical conductivity under external stimuli.

In order to extend the nature of the EBS, we have also studied the electronic energy density of states (total and partial density of states) of the titled compounds as shown in Figure 3. Considering the hybrid functional of HSE06, the lowest-energy parts of the CB for $B_{12}S$ ($B_{12}Se$) at 2.30 (1.30) eV are formed by the strong hybridization of s and p orbitals of the B element, while hybridization between s and p orbitals of the S element has a minor contribution. On the other hand, the highest-energy parts of the VB in the vicinity of E_F are mainly constructed by the hybridization of p orbitals of both B and S/Se elements.

It can be seen here from the PDOS plots that hybridization of B and Se p orbitals is much stronger than that between B and S orbitals, resulting in a shift of the lowest conduction band downward (lower energy). Similar qualitative features could be found for both the titled chalcogenides using LDA and GGA functionals to model the exchange and correlation effects.

The three-dimensional (3D) mapping images of charge density distributions of $B_{12}S$ and $B_{12}Se$ are depicted in Figure 4. It can be deduced from the figures that there are asymmetric charge distributions in the studied compounds owing to the difference in the electronegativity of S and Se atomic species. The depletion of charge density indicated by the blue color is found around S/Se atoms, while the accumulation of charge is pointed out by the red color as seen around the B atomic species. This reflects that the charge (electron) is shifted from the S/Se element to the B element, which is suggestive of ionic bonding. In addition to this, strong covalent bonds between B−B and B−S/Se atoms are found owing to the directional accumulation of charge. The charge density distributions in both studied compounds are different as seen from charge accumulation and depletion regions. In the $B_{12}Se$ compound, charge accumulation around B atoms and depletion around the Se element are more pronounced than those in the $B_{12}S$ compound. This suggests that the amount of charge transfer as well as bonding strength could be different in these boron-rich compounds,[35] which is also confirmed from the study of Mulliken population analysis as shown in Table 3. The B and S/Se atoms have a negative and positive charge, respectively. The transfer of charge from S to B atoms in the $B_{12}S$ compound is 0.08|e|, while in the $B_{12}Se$ compound, it is from Se to B atoms and is 0.22|e| and 0.10|e| as indicated in Table 3.

https://doi.org/10.1021/acsomega.1c05172
ACS Omega 2021, 6, 33899−33913

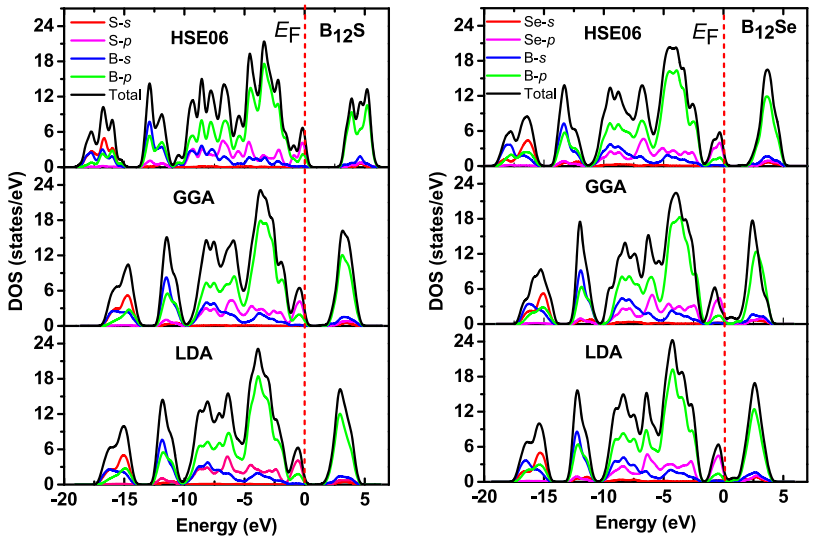

Figure 3. Density of states (total and partial) of boron-rich chalcogenide compounds $B_{12}S$ and $B_{12}Se$ using LDA, GGA, and HSE06 functionals. The red dashed vertical lines denote the Fermi level (E_F) set to 0 eV.

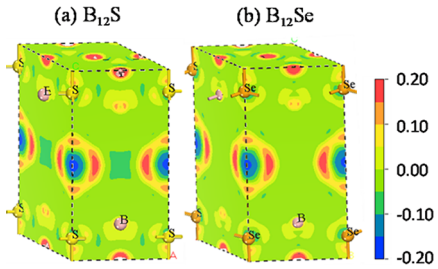

Figure 4. 3D mapping images of charge density distributions of the titled chalcogenides: (a) $B_{12}S$ and (b) $B_{12}Se$ compounds. The adjacent scale shows the charge value (in the units of electronic charge) from −0.2 to +0.2.

Table 3. Estimated Mulliken Atomic Population of Boron-Rich Chalcogenides $B_{12}X$ (X = S and Se)[a]

compound	atom	s	p	total	charge (e)	EVC (e)
$B_{12}S$	B	0.83	2.17	3.00	0.00	
	B	0.79	2.29	3.08	−0.08	
	S	1.59	4.17	5.76	0.24	5.76
$B_{12}Se$	B	0.88	2.22	3.10	−0.10	
	B	0.85	2.36	3.22	−0.22	
	Se	0.97	4.08	5.05	0.95	5.05

[a]Here, EVC indicates the effective valence charge.

These results are consistent with the results of charge density distribution mapping.

3.3. Optical Properties. In order to evaluate the feasibility of a material for possible optoelectronic and photonic device applications as well as for the characterization of materials, especially semiconducting properties, it is of paramount importance to study various optical features first. Generally, the optical property is related to a material's response when electromagnetic radiation, particularly visible light, is exposed on it. Some important optical devices such as LCD screens, screens for 3D movies, polarizers, and wave plates, to name a few, are fabricated based on the properties of optical anisotropy.[6,20,36] Therefore, the optical properties along with anisotropy in a broad spectral range are of decisive interest to extend their application scope. In the present investigation, the optical properties as well as optical anisotropy of two titled compounds are studied in the photon energy range up to 15 eV for two polarization directions [100] and [001], for the first time. It is interesting to note here that the shapes of the spectrum and energy peak position for all optical properties are different and distinguishable with respect to the polarization direction of the incident electric field. The direction-dependent real $[\varepsilon_1(\omega)]$ and imaginary $[\varepsilon_2(\omega)]$ parts of the dielectric function for both compounds are illustrated in Figure 5. It is seen that large anisotropic behavior of both dielectric functions is observed in the IR, visible, and mid-UV region up to 12 eV. Particularly, the very strong anisotropic nature of these dielectric functions in the IR and visible region is crucially important for efficient light manipulation in many devices. Following the Penn model,[37,38] the static value of the dielectric constant $[\varepsilon_1(0)]$ can be evaluated from the plasma energy (E_p), Fermi energy (E_F), and energy band gap (E_g) as follows:

$$\varepsilon_1(0) = 1 + \left(\frac{E_p}{E_g}\right)^2\left[1 - \frac{E_g}{4E_F} + \frac{1}{3}\left(\frac{E_g}{4E_F}\right)^2\right]$$

The static value of $[\varepsilon_1(0)]$ that describes the index of refraction is also necessary to design many optical devices. For $B_{12}Se$, the highest values of $[\varepsilon_1(0)]$ are calculated using the GGA (HSE06) functional and found to be 5.08 (3.51) and 4.75 (3.23) for the [100] and [001] polarizations, respectively, while the corresponding values are 4.75 (3.41) and 4.07 (3.05) for $B_{12}S$ for the [100] and [001] polarization directions, respectively. The $[\varepsilon_1(\omega)]$ for both the compounds using the GGA (HSE06) functional gradually increased with photon energy, reaching the highest values of 7.75 (5.36) at 5.2 (6.2) eV for $B_{12}S$ and 8.20 (6.04) at 5.22 (6.16) eV for $B_{12}Se$ for the [100] direction and finally going to zero at around 6.5 (7.5) eV energy. The photon energy/frequency-dependent imaginary part of the dielectric constant $[\varepsilon_2(\omega)]$ signifies the light absorption of the material. The values of $[\varepsilon_2(\omega)]$ for $B_{12}S$ using the GGA (HSE06) functional started at incident photon energies of 1.9 (2.56) and 1.8 (2.77) eV along the [100] and [001] directions, respectively, and for $B_{12}Se$, the values are 1.35 (2.40) and 1.0 (2.30) eV for the same. The major peaks observed in $[\varepsilon_2(\omega)]$ for both chalcogenides arise due to the

https://doi.org/10.1021/acsomega.1c05172
ACS Omega 2021, 6, 33899−33913

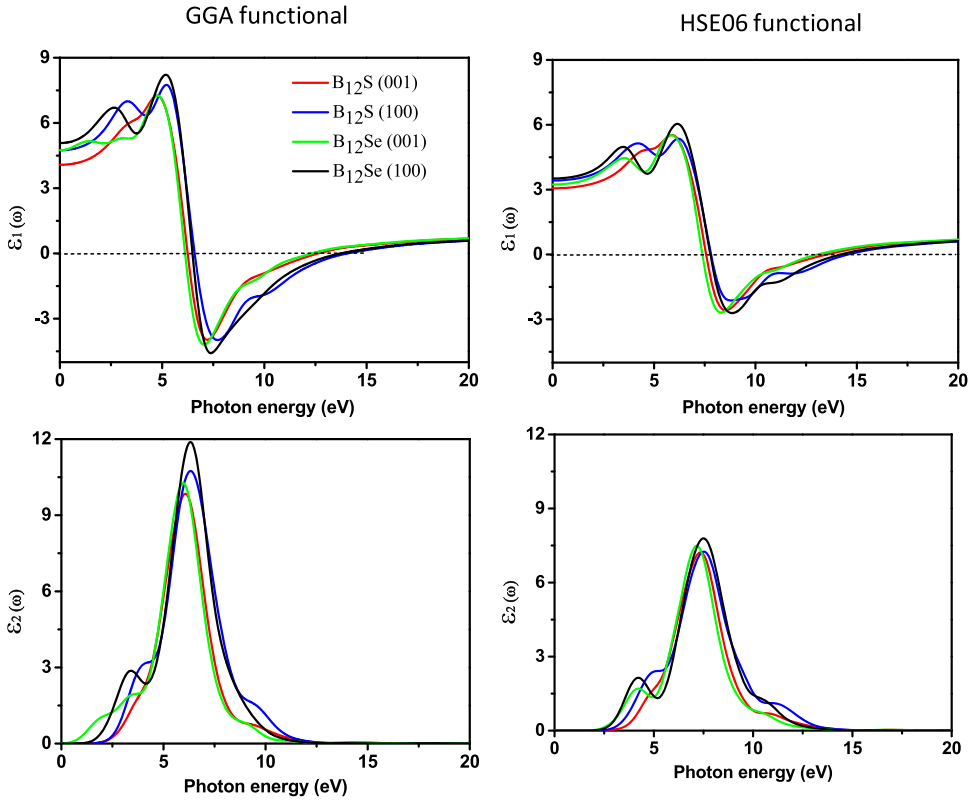

Figure 5. Photon energy-dependent dielectric functions (real part $[\varepsilon_1(\omega)]$ and imaginary part $[\varepsilon_2(\omega)]$) of boron sub-sulfide ($B_{12}S$) and boron sub-selenide ($B_{12}Se$) compounds along different polarization directions of electric fields using the GGA and hybrid HSE06 functionals.

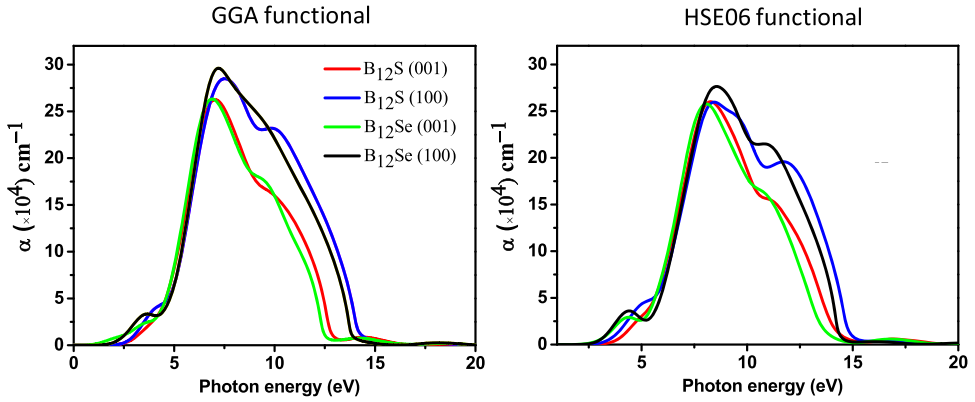

Figure 6. Computed optical absorption coefficients, $\alpha(\omega)$, of boron sub-sulfide ($B_{12}S$) and boron sub-selenide ($B_{12}Se$) compounds for different polarization directions of the electric field using GGA and hybrid HSE06 functionals.

optical transition mainly from the highest energy of the valence band of S/Se p orbitals to the lowest energy of the conduction band of B p orbitals. The positions of prime peaks are varied along different polarization directions with photon energy, which is a clear signature of the optical anisotropy, as depicted in Figure 5.

The optical absorption coefficient, $\alpha(\omega)$, can be computed using the formula mentioned in the theoretical methodology (Section 2). Figure 6 shows the energy-dependent absorption coefficient curves for the two polarization directions [100] and [001]. It is noticed that the $\alpha(\omega)$ revealed strong anisotropy along the [100] and [001] polarization directions, and in particular, large anisotropy in the absorption coefficient is observed in the visible and UV spectrum (up to ∼5.0 eV), and then, anisotropy is drastically reduced at an energy of around 8 eV. Interestingly, bulk absorption anisotropy is again observed in the deep-UV region within an energy range of 8.0−14.5 eV. Since the visible-light absorption coefficient as well as anisotropy is very important to design an optical device,[36] we are more interested to put deep insight in this aspect. Figure 7 shows the enlarged spectrum in the visible region. It is obvious that the spectrum of $\alpha(\omega)$ along the [100] directions has a blueshift in comparison to that along the [001] polarization directions for both the boron-rich semiconductors. This implies that strong visible-light absorption should be found along the in-plane direction.

Therefore, the boron sub-sulfide ($B_{12}S$) and boron sub-selenide ($B_{12}Se$) compounds as an optical absorber in photovoltaic devices, for example, should be used parallel to the optical source in order to achieve the best absorption

https://doi.org/10.1021/acsomega.1c05172
ACS Omega 2021, 6, 33899−33913

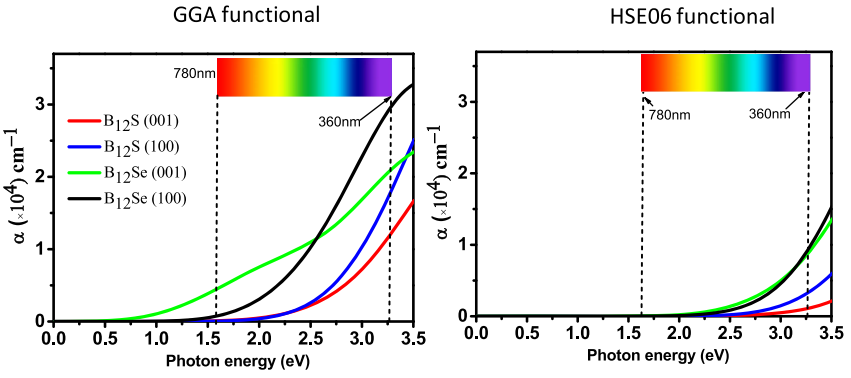

Figure 7. Enlarged figures of absorption coefficient, $\alpha(\omega)$, spectra in the visible spectrum for $B_{12}S$ and $B_{12}Se$ compounds using GGA and hybrid HSE06 functionals.

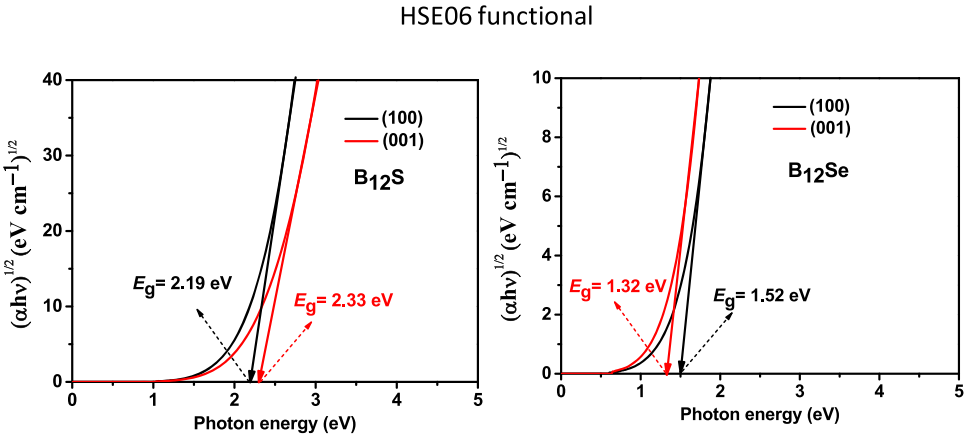

Figure 8. Estimation of the optical band gap from the absorption coefficient, $\alpha(\omega)$, spectrum using the Tauc plot for $B_{12}S$ and $B_{12}Se$ compounds using the hybrid HSE06 functional.

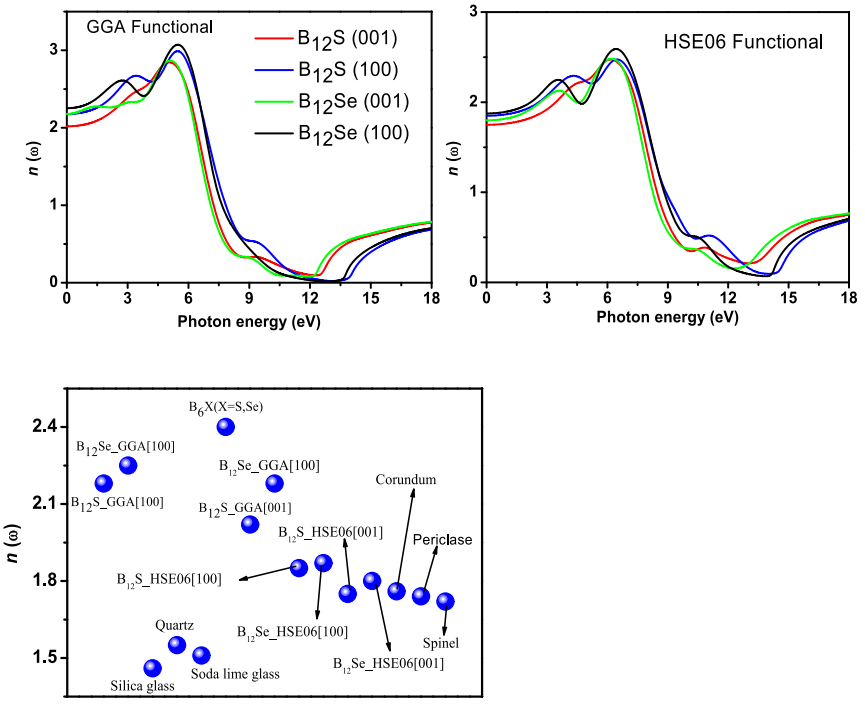

Figure 9. Refractive index spectra, n, of $B_{12}S$ and $B_{12}Se$ compounds obtained using the GGA and hybrid HSE06 functionals as a function of incident photon energy. Lower panel: comparison of the static refractive index, $n(0)$, of $B_{12}S$ and $B_{12}Se$ with some other well-known ceramic and optical waveguide materials.

https://doi.org/10.1021/acsomega.1c05172
ACS Omega 2021, 6, 33899−33913

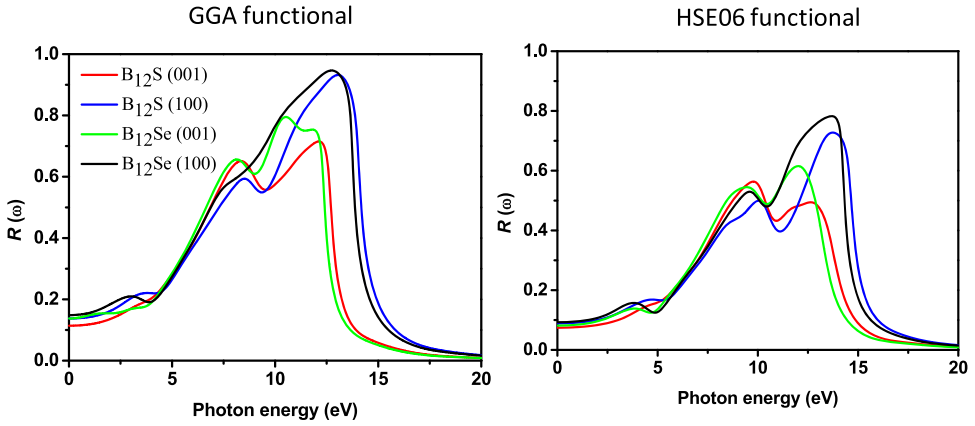

Figure 10. Reflectivity spectra of boron sub-sulfide ($B_{12}S$) and boron sub-selenide ($B_{12}Se$) compounds plotted as a function of photon energy.

efficiency.[35] The major peaks of $\alpha(\omega)$ using the GGA (HSE06) functional are noticed at 7.56 (8.44) and 7.00 (8.26) eV for $B_{12}S$, and they are at 7.16 (8.56) and 7.00 (8.06) eV for the $B_{12}Se$ compound for the [100] and [001] directions, respectively. The maximum value of $\alpha(\omega)$ in the visible-light region using the GGA (HSE06) functional is $\sim 3 \times 10^4$ (1×10^4) cm^{-1} for the $B_{12}Se$ compound. The optical band gap can also be determined for both the studied chalcogenides using the well-known Tauc plot from absorption coefficient spectra.[39] An accurate estimation of optical band gap energy is quite important to predict some features such as the photophysical and photochemical properties of semiconducting materials. On the other hand, wrong use of the Tauc plot to estimate this band gap energy provides misinformation, and in particular, error in estimation of the band gap can reflect the light absorption within the sub-band gap energy.[40] However, the Tauc equation, which is based on the absorption coefficient, can be written as follows: $(\alpha \cdot h\nu)^{1/\eta} = A(h\nu - E_g)$ where α, h, ν, A, and E_g signify the absorption coefficient, Planck constant, frequency, a material-dependent coefficient, and the band gap, respectively.[39] The value of parameter η depends on the nature of the band gap, and in general, 1/2 and 2 are used for direct and indirect band gap semiconductors, respectively. Figure 8 illustrates the optical band gap energy estimation using the Tauc plot for both the chalcogenides under consideration. It is found that the obtained optical band gaps for $B_{12}S$ and $B_{12}Se$ compounds are 2.19 (2.33) and 1.52 (1.32) eV, respectively, for the [100] ([001]) direction calculated using the HSE06 functional. The optical band gaps are consistent with those obtained from the electronic band structure gaps as shown in Figure 2 and Table 2.

The refractive indices are also studied to further check the suitability of the two compounds in optoelectronic devices. When a light wave (photons) penetrates through a material, its electric field interacts with the electrons of solids and the real part of the refractive index measures how the velocity of the light wave is modified compared to its free-space value. It is seen in Figure 9 that the value of n is also dependent on the polarization directions of the incident electric fields as the static values of $n(0)$ at zero frequency using the GGA (HSE06) functional along the [100] ([001]) direction are 2.17 (1.84) and 2.01 (1.75) for $B_{12}S$ and 2.25 (1.87) and 2.17 (1.80) for $B_{12}Se$. Since the value of n is different in different directions, the effective refractive index must be dependent on the electric field direction of light. However, the variations of these values in the visible-light region are not that prominent, rather reasonably constant. The electric polarization-dependent value of n also suggests that a higher value of n[100] results due to the highest density of ions along these directions.[36] The value of n considering the HSE06 functional is lower than those of B_6X (X = S and Se),[6] $NaInSe_2$,[20] MAX,[41,42] and MAB[43−45] but is slightly higher than those of some ceramic materials such as silica glass, quartz, and soda lime glass and, in some compounds, very close to those of corundum, periclase, and spinel.[46] A comparison of n (at 0 eV) with some well-known optical waveguide materials is presented in the lower panel of Figure 9. This comparison implies that the titled compounds are likely to be useful as optical guides.

The reflectivity spectra of boron sub-sulfide and sub-selenide are estimated and plotted as a function of photon energy in Figure 10. It is found that the reflectivity spectrum is very sensitive in the IR-, visible-, and UV-light (up to 5.0 eV) regions when the electric field polarization is along the [100] and [001] directions. Like the anisotropic behavior of the absorption coefficient, the anisotropy of the reflectivity spectra was also drastically reduced in the photon energy range of 5.0−8.0 eV, and then, again, at higher energies, the anisotropic nature is prominently noticed. The starting values of the spectra for $B_{12}S$ are 0.0888 (0.14) and 0.0742 (0.113) for the [100] and [001] directions, respectively, calculated using the HSE06 (GGA) functional. On the other hand, the starting values for $B_{12}Se$ are 0.0925 (0.1483) and 0.0815 (0.1375) for the same. Polarization direction-dependent maximum reflectivity spectra are seen for both the functionals in the following sequence: $B_{12}Se[100] > B_{12}S[100] > B_{12}Se[001] > B_{12}S[001]$ at various incident photon energies as shown in Figure 10.

The transparency $T(\omega)$ of any material can be estimated with the help of the absorption coefficient, $\alpha(\omega)$, and reflectivity, $R(\omega)$, data as follows:[33]

$$T(\omega) = (1 - R(\omega))e^{-\alpha(\omega)t}$$

ω and t are the light frequency and thickness of the material, respectively. Lower values of the absorption coefficient or the reflectivity result in the higher value of the transparency as indicated from the above equation. It is worth noticing from Figures 10 and 6 that the reflectivity spectra and absorption coefficients of both the compounds have the values of reflectivities and absorption coefficients of ∼10.0% and ∼1.0 $\times 10^4$ cm^{-1}, respectively, at least in the visible-light region.

https://doi.org/10.1021/acsomega.1c05172
ACS Omega 2021, 6, 33899−33913

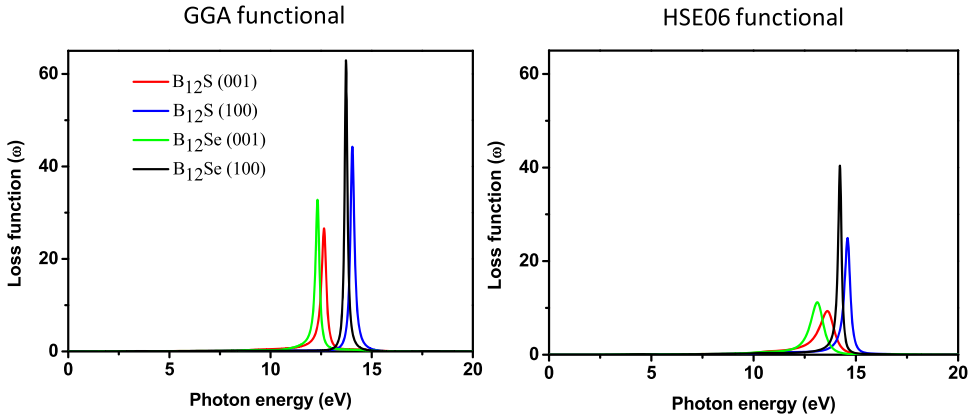

Figure 11. Photon energy-dependent loss functions of boron sub-sulfide ($B_{12}S$) and boron sub-selenide ($B_{12}Se$) compounds.

Table 4. Calculated Stiffness Constants (GPa), Elastic Moduli (*B*, *G*, and *Y*; All in GPa), Poisson's Ratio (υ), Pugh's Ratio (*G*/*B*), Hardness Values (H_{Chen}, H_{Miao}, and $H_{Mazhnik}$; All in GPa), and Fracture Toughness, K_{IC} ($MPam^{0.5}$), of Boron-Rich Chalcogenide $B_{12}X$ (X = S and Se) Compounds with a Hexagonal Structure

phase		C_{11}	C_{33}	C_{44}	C_{12}	C_{13}	C_{14}	B	G	Y	υ	G/B	H_{Chen}	H_{Miao}	$H_{Mazhnik}$	K_{IC}
$B_{12}S$	GGA	463	352	119	108	54	30	187	148	351	0.18	0.79	25.29	30.89	20.32	4.27
	LDA	487	371	121	124	61	35	201	151	362	0.19	0.75	23.93	30.24	19.27	4.55
$B_{12}Se$	GGA	386	313	86	151	46	56	171	096	243	0.26	0.56	11.69	15.13	11.57	3.13
	LDA	437	336	99	134	51	36	183	126	307	0.22	0.68	18.88	23.52	14.56	3.80

This indicates that the titled chalcogenide compounds are fairly transparent materials.

The loss function, $L(\omega)$, is related to the loss of energy of charged particles (e.g., electrons) when they travel through a material. It can be seen from Figure 11 that the energy loss of electrons is prominently seen in the mid-UV region (within the energy range of 12−15 eV for both the compounds). Very sharp peaks are attained at the plasma frequency. The plasma resonances using the GGA (HSE06) functional are at 14.04 (14.6) and 12.64 (13.60) eV for $B_{12}S$ and at 13.72 (14.22) and 12.31 (13.11) eV for $B_{12}Se$, along the [100] and [001] polarization directions, respectively. Additionally, it can be seen that there are no $L(\omega)$ peaks in the range of 0−12 eV owing to the high value of $[\varepsilon_2(\omega)]$.[47] The imaginary part of the dielectric function is greatly suppressed at the plasma resonance.

It is found that like other optical properties discussed herein, the energy loss function for both the compounds could be higher along with a larger plasmon energy when for the [100] polarization in comparison to that for the [001] direction. Prior to the present study, there has been no experimental and/or theoretical report concerning the optical properties of $B_{12}S$ and $B_{12}Se$ to validate our theoretical estimations. The results reported in this section will require future experimental verification.

3.4. Mechanical Properties and Hardness. In order to comprehend the mechanical behaviors of the two compounds, we have calculated the parameters characterizing mechanical properties such as elastic constants (C_{ij}), elastic moduli, hardness parameters, brittle/ductile behavior, etc. The calculation of elastic constants C_{ij} via the CASTEP code was performed using an efficient stress−strain method.[48,49] The stress−strain relationship is usually expressed by the generalized Hooke's law: $\sigma_{ij} = C_{ijkl}\varepsilon_{kl}$. Here, the fourth-order elastic stiffness tensor C_{ijkl} contains 81 components, and σ_{ij} and ε_{kl} are the second-order stress tensor and strain tensor, respectively. The 6 × 6 matrix can be used to express the fourth-order tensor using the Voigt markers, the equation can be simplified to $\sigma_i = C_{ij}\varepsilon_j$, as $C_{ij} = C_{ji}$, and the number of independent components in the elastic stiffness tensor can be reduced to 21. Due to the symmetry of the crystal structure, the number of single-crystal elastic constants is different for different crystal systems.

Since neither experimental nor theoretical data of the elastic properties of both the titled phases are available, thus, a comparison between the values obtained for different functionals can be useful to predict the reliability of our calculations. The values of elastic constants and elastic moduli show an opposite trend to that of the lattice constants, i.e., LDA (GGA) gives lower (higher) lattice constants that result in higher (lower) elastic parameters, as expected. It is also proven that LDA and GGA give higher and lower values of elastic constants, respectively.[50] This inspires us to calculate the elastic properties using these functionals with the hope that the exact values of the elastic parameters for $B_{12}S$ and $B_{12}Se$ should remain within this limit. Table 4 enlists the obtained parameters used to describe the mechanical behaviors of the considered compounds. One of the decisive pieces of information that can be revealed from the obtained elastic constants (C_{ij}) is the confirmation of the mechanical stability of the studied materials. The conditions of mechanical stability for hexagonal systems are as follows: $C_{11} > 0$, $C_{11} > C_{12}$, $C_{44} > 0$, and $(C_{11} + C_{12})C_{33} - 2(C_{13})^2 > 0$.[51] It is obvious from Table 4 that the obtained values of C_{ij} satisfy the mentioned criteria, and hence, both the compounds are mechanically stable. Some more useful information can be extracted from the values of C_{ij}. As evident from Table 4, C_{11} is larger than C_{33} for both functionals. As C_{11} and C_{33} are directly related to atomic bonds along the $x(y)$ and z axes, respectively, the atoms along the $x(y)$ axis are bonded strongly compared to those along the z axis for both the phases. Table 4 reveals that C_{11} and C_{33} of $B_{12}S$ are larger than those of $B_{12}Se$, indicating a higher

https://doi.org/10.1021/acsomega.1c05172
ACS Omega 2021, 6, 33899−33913

resistance to axial deformation of $B_{12}S$ in comparison with $B_{12}Se$. Another elastic constant, C_{44}, usually used to measure the shear deformation resistance, is also much higher for $B_{12}S$ than that of $B_{12}Se$, implying a higher shear deformation resistance of $B_{12}S$ compared to $B_{12}Se$. The unequal values of C_{11} and C_{33} also reveal the difference in the atomic arrangements along the $x(y)$ and z axes. Such an arrangement of atoms is desired for hexagonal systems to ensure the minimum energy of the system in the ground state; consequently, the density of atoms along the $x(y)$ and z axes is different that results in different values of C_{11} and C_{33}. In addition, C_{11} and C_{33} are larger than C_{12}, C_{13}, and C_{14}, implying that shear deformation is easier than axial deformation for both the boron-rich phases. Moreover, the unequal values of C_{11} and C_{33} and C_{12}, C_{13}, and C_{14} reveal the anisotropy in the elastic moduli (Y, B, and G). Finally, the elastic constants are used to calculate the macroscopic elastic moduli and ratios such as the bulk modulus (B), shear modulus (G), Young's modulus (Y), and Poisson's ratio (υ) using the Voigt−Reuss−Hill (VRH) approximation.[52−54] The required expressions for these calculations can be found elsewhere.[6,55,56] The obtained values are listed in Table 4 from which it is seen that the B, G, and Y are 187, 148, and 351 GPa and 171, 96, and 243 GPa for $B_{12}S$ and $B_{12}Se$, respectively, obtained using the GGA functional. As B, G, and Y measure the volume deformation resistance, shear deformation resistance, and stiffness of solids, $B_{12}S$ exhibits strong volume and shear deformation resistances as well as strong stiffness compared to $B_{12}Se$.

Next, we discuss the brittle/ductile behavior of the studied compounds. Brittleness/ductility is a decisive property for application purposes. The related parameter can be obtained based on the Poisson's ratio (υ) and Pugh's ratio (G/B). The υ and G/B have an opposite tendency to their values owing to the interdependence of the polycrystalline elastic parameters. The Poisson's ratio, used to measure the lateral structural deformation during the stretching or compression, is widely used to predict the ductility or brittleness of solids with a critical value of υ ~0.26 (for brittle materials, $\upsilon < 0.26$, and for ductile materials, $\upsilon > 0.26$).[57−60] As predicted from the calculated values in Table 4, $B_{12}S$ should behave as a brittle material, whereas for $B_{12}Se$, the Poisson's ratio has values of 0.26 and 0.22 using the GGA and LDA functionals, respectively. Thus, we can define $B_{12}Se$ as a quasi-brittle material. Again, for the Pugh's ratio (G/B), the critical value used to separate ductile and brittle behavior is 0.57 [for brittle materials, $G/B > 0.57$, and for ductile materials, $G/B < 0.57$].[61] Like the Poisson's ratio, the Pugh's ratio also classifies $B_{12}S$ as a brittle solid. For $B_{12}Se$, G/B has values of 0.56 and 0.68 using the GGA and LDA functionals, respectively, which again directs us to define $B_{12}Se$ as a quasi-brittle material. It is encouraging to find that results from both the indicators are fully consistent with each other.

Furthermore, we have calculated the hardness parameters using three well-established models, namely, Chen et al.'s model,[62] Miao et al.'s model,[63] and Mazhnik and Oganov's model[64] using USPEX.[65] The results are given in Table 4. As can be seen from Table 4, the hardness parameters are higher for $B_{12}S$ than those for $B_{12}Se$. Among the mechanical characterizing parameters, C_{44} is assumed to be the best hardness predictor parameter.[66] The value of C_{44} for $B_{12}S$ is 119 GPa using GGA, 121 GPa using LDA. These values are much higher than those of $B_{12}Se$ (86 GPa using GGA, 99 GPa using LDA). Therefore, higher values of hardness parameters are expected for $B_{12}S$ compared to $B_{12}Se$. The higher hardness values of $B_{12}S$ compared to $B_{12}Se$ can also be explained on the basis of the DOS as shown in Figure 12. Red rectangles are

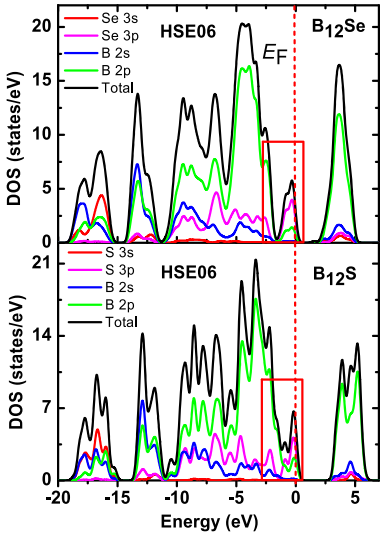

Figure 12. Total and partial DOS for $B_{12}S$ and $B_{12}Se$ compounds as a function of electron energy. Red rectangles are drawn in the figure showing the difference in the values of DOS for both the compounds.

drawn in the figure in which there is a large difference in the values of TDOS for $B_{12}S$ and $B_{12}Se$. As seen, a peak in the DOS very close to the Fermi energy (E_F) is decreasing to a certain value (2.30 states/eV), and then, there is an upturn to exhibit another peak in the lower-energy part for $B_{12}S$. On the other hand, the peak close to E_F is reduced to almost zero (0.38 states/eV), and then, the upturn exhibits another peak in the lower-energy part for $B_{12}Se$. In this region, a strong hybridization between B 2p and S/Se 3p electronic orbitals is observed that leads to the formation of covalent bonds between B and S/Se atoms. The strength of this hybridization depends largely on the value of the density of states: when more states are involved in the hybridization, the covalent bond formed is stronger. Thus, the covalent bond formed between B and S in this region is much stronger than the covalent bond formed between B and Se atoms in this energy region. Therefore, a higher value of hardness is expected for $B_{12}S$ compared to $B_{12}Se$, which is reflected well in the values presented in Table 4.

Now, we can compare the obtained values of hardness for titled compounds with some other B-rich compounds (ZrB_{12}, HfB_{12}, YB_{12}, LuB_{12},WB_{12}, and TiB_{12}). Korozlu et al.[12] have reported hardness values (using Gao et al.'s model[67]) of 40.1, 39.1, 36.5, and 32.3 GPa for ZrB_{12}, HfB_{12},YB_{12}, and LuB_{12}, respectively. However, Pan and Jia[13] have reported hardness values of 29.9 and 43.2 GPa for WB_{12} and TiB_{12}, respectively, using Miao's model. The hardness values of the above mentioned compounds are higher than those of our considered compounds. Some of them can be considered as superhard materials with hardness greater than 40 GPa (ZrB_{12} and TiB_{12}), and the rest of them are considered as hard materials. We have also studied some B-rich compounds (B_6X; X = S and Se) with hardness values of 33.60 and 35.57 GPa (using Chen's formula) and categorized them as hard materials. Mazhnik and Oganov[64] have also calculated the hardness of widely known hard materials such as B_4C (32.6 GPa), B_6O

https://doi.org/10.1021/acsomega.1c05172
ACS Omega 2021, 6, 33899−33913

Table 5. Calculated Values of Different Anisotropy Indices: Shear Anisotropy Factors (A_{100}, A_{010}, and A_{001}), Anisotropy in the Bulk Modulus (B_a and B_c), Compressibility (k_c/k_a), Percentage Anisotropy (A_B and A_G), and the Universal Anisotropy Index A^U of Boron-Rich Chalcogenide $B_{12}X$ (X = S and Se) Compounds

phases	A_{100}	A_{010}	A_{001}	B_a	B_c	k_c/k_a	A_B	A_G	A^U
$B_{12}S$	1.48	0.67	0.99	655	422	1.55	1.52	4.02	0.45
$B_{12}Se$	1.90	0.73	1.39	614	368	1.67	2.11	19.52	2.46

(35.5 GPa), β-SiC (34.8 GPa), SiO_2 (30.0 GPa), WC (33.5 GPa), OsB_2 (17.8 GPa), VC (26.5 GPa), Re_2B (38.6 GPa), etc. It is seen that the calculated values of hardness for both the titled compounds using the aforementioned three models are significantly varied, ranging within 19−31 and 11−24 GPa for $B_{12}S$ and $B_{12}Se$, respectively. Very recently, Solozhenko[15] measured the microhardness of these compounds experimentally using Vicker hardness (H_V) and Knoop hardness (H_K) methods. The obtained values for $B_{12}S$ and $B_{12}Se$ compounds are 32 and 33 GPa using the H_V method, whereas they are 26 and 22 GPa using the H_K method, respectively. In our case, the calculated hardness using the H_{Miao} model is reasonably consistent with experimental Knoop hardness values. Thus, by comparing the hardness values of the titled chalcogenides with those of the other mentioned compounds, we classify $B_{12}S$ as a potential hard material. However, the hardness of $B_{12}Se$ is slightly lower than those of all the other compounds, and it is likely to be a hard material.

For hard materials, fracture toughness (K_{IC}) also carries significance like hardness for practical applications of solids.[68] Fracture may occur within a solid under extreme conditions of external stress. In such cases, prior information regarding fracture toughness is crucially important because it provides the required guideline for use and gives a measure of the resistance of solids to stop the propagation of the induced fracture inside. A high value of fracture toughness is expected for hard materials for use in industrial purposes, and evaluation of the K_{IC} receives significant scientific concerns.[69−71] The obtained values of the hardness parameters inspire us to study the K_{IC} of $B_{12}X$ (X = S and Se) using the formula $K_{IC} = V_0^{1/6} \cdot G \cdot (B/G)^{1/2}$.[64] The calculated values of K_{IC} are 4.27 and 3.13 $MPam^{0.5}$ for $B_{12}S$ and $B_{12}Se$, respectively, using the GGA, while they are 4.55 and 3.80 $MPam^{0.5}$ obtained using the LDA. These values are higher than those of B_6S (2.070 $MPam^{0.5}$) and B_6Se (2.072 $MPam^{0.5}$).[6] Moreover, Mazhnik and Oganov[64] have also reported the K_{IC} of superhard diamond (6.3 $MPam^{0.5}$), WC (5.4 $MPam^{0.5}$), and c-BN (5.4 $MPam^{0.5}$), which are higher than those of $B_{12}S$ and $B_{12}Se$. Overall, the fracture hardness values of boron-rich $B_{12}S$ and $B_{12}Se$ are reasonably high.

The hard materials are suitable for structural components in different sectors, but one of the great problems is their low level of machinability. A hard material with a higher machinability is a great combination for engineering applications. Thus, information regarding the machinability index (MI) calculated using the B/C_{44} ratio is crucial for predicting applications of hard materials.[6,45] The obtained values of the MI are 1.57 (1.66) and 1.98 (1.85) for $B_{12}S$ and $B_{12}Se$ using the GGA (LDA) functional. These values are higher than those of B_6S and B_6Se. These values are also higher than those of some well-known machinable MAX phases,[45] which predict that $B_{12}S$ and $B_{12}Se$ might be quite machinable.

The melting temperature, T_m, is estimated for both the studied chalcogenides using the following formula: $T_m = 412 + (8.2 \times C_{11})$.[72] The obtained values of T_m are 4208 (4405) and 3577 (3995) K for $B_{12}S$ and $B_{12}Se$ compounds using the GGA (LDA) functional, respectively. These values are higher than those of B_6S and B_6Se.[6] The compound $B_{12}S$ has a higher T_m than $B_{12}Se$, and considering the computational uncertainty for using different functionals, it can be stated that the $B_{12}S$ and $B_{12}Se$ compounds should be stable at least up to 4208 and 3577 K, respectively, which are much higher values than the synthesis temperature of 2500 K.[8] According to the Born criterion,[73] the T_m of a material is related to the shear modulus (G) as well as the elastic stiffness constant C_{44}. Melting of a material starts when G vanishes and the material becomes elastically unstable.[74] Higher values of G and C_{44} correspond to the higher value of T_m. Our calculated values of T_m for both the compounds are consistent with the estimated G and C_{44} values as shown in Table 4.

3.5. Elastic Anisotropy. Elastic anisotropy should be taken into account for full description of the mechanical properties of solids, especially for hexagonal symmetry where the atomic arrangement varies largely along the $a(b)$ and c axes. Moreover, it is also closely associated with unusual phonon modes, dislocation dynamics, precipitation, plastic deformation in solids, and microscale crack creation.[75−77] Thus, information regarding elastic anisotropy of solids is very important for use in materials engineering and in crystal physics. Unfortunately, no unique method has been developed to measure the degree of anisotropy yet, and for this reason, we have used different models that are widely used.

First of all, we started with the calculation of shear anisotropy factors that are defined for hexagonal solids like $B_{12}S$ and $B_{12}Se$ as follows: $A_1 = \frac{\frac{1}{6}(C_{11} + C_{12} + 2C_{33} - 4C_{13})}{C_{44}}$, $A_2 = \frac{2C_{44}}{C_{11} - C_{12}}$, $A_3 = A_1 \cdot A_2 = \frac{\frac{1}{3}(C_{11} + C_{12} + 2C_{33} - 4C_{13})}{C_{11} - C_{12}}$[78] for the {100}, {010}, and {001} planes in between ⟨011⟩ and ⟨010⟩, ⟨101⟩ and ⟨001⟩, and ⟨110⟩ and ⟨010⟩ directions, respectively. A unity (1) value of $A_{\{100\}}$, $A_{\{010\}}$, and $A_{\{001\}}$ indicates the completely isotropic nature otherwise. Values deviating from unity imply anisotropy. The degree of deviation measures the level of anisotropy. The calculated shear anisotropy factors are listed in Table 5, which shows that $B_{12}S$ and $B_{12}Se$ are anisotropic solids.

The anisotropy in the bulk modulus and compressibility are defined as follows: $B_a = a\frac{dP}{da} = \frac{\Lambda}{2 + \alpha}$ and $B_c = c\frac{dP}{dc} = \frac{B_a}{\alpha}$,where B_a and B_c are bulk moduli along the a and c axes, $\Lambda = 2(C_{11} + C_{12}) + 4C_{13}\alpha + C_{33}\alpha^2$, and $\alpha = \frac{(C_{11} + C_{12}) - 2C_{13}}{C_{33} - C_{13}}$,[78] and $\frac{k_c}{k_a} = C_{11} + C_{12} - 2C_{13}/(C_{33} - C_{13})$, where k_a and k_c are the compressibilities along the a and c axes, respectively. The listed values (Table 5) of B_a and B_c ($B_a = B_c$ for isotropic nature) and k_c/k_a ($k_c/k_a = 1$ for isotropic nature) confirmed the anisotropic nature of $B_{12}S$ and $B_{12}Se$.

Chung and Buessem[79] have introduced the percentage anisotropy in compressibility and shear, which are defined as

https://doi.org/10.1021/acsomega.1c05172
ACS Omega 2021, 6, 33899−33913

Table 6. The Minimum and the Maximum Values of the Young's Modulus (Y), Compressibility (K), Shear Modulus (G), and Poisson's Ratio (υ) of $B_{12}S$ and $B_{12}Se$ Compounds

phases	$Y_{min.}$ (GPa)	$Y_{max.}$ (GPa)	A_Y	$K_{min.}$ (TPa^{-1})	$K_{max.}$ (TPa^{-1})	A_K	$G_{min.}$ (GPa)	$G_{max.}$ (GPa)	A_G	$\upsilon_{min.}$	$\upsilon_{max.}$
$B_{12}S$	265.16	448.71	1.69	1.52	2.37	1.55	105.76	190.17	1.79	0.006	0.340
$B_{12}Se$	119.67	385.62	3.22	1.63	2.72	1.66	43.30	160.36	3.70	−0.23	0.85

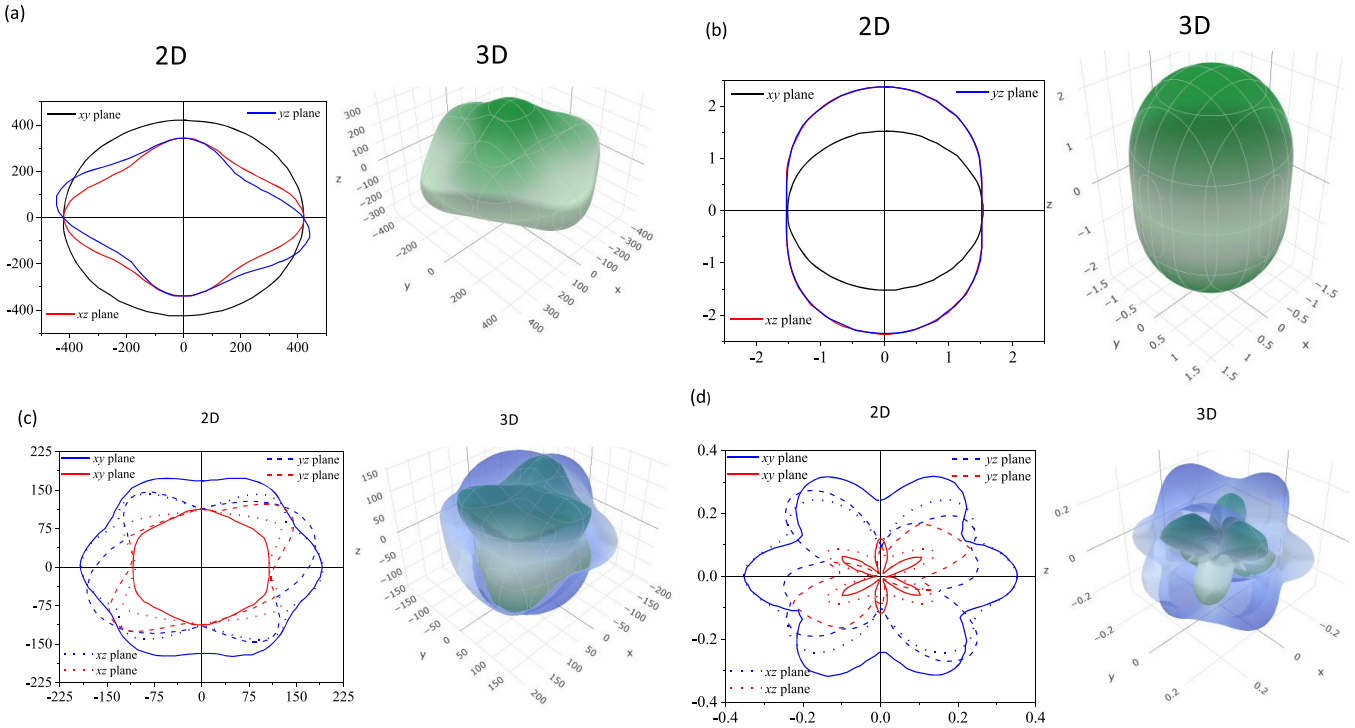

Figure 13. 2D view and 3D view of (a) Young's modulus (Y), (b) compressibility (K), (c) shear modulus (G), and (d) Poisson's ratio (υ) for the chalcogenide $B_{12}S$ indicating the degree of anisotropy.

follows: $A_B = \frac{B_V - B_R}{B_V + B_R}$ and $A_G = \frac{G_V - G_R}{G_V + G_R}$. For isotropic solids, A_B (A_G) = 0; otherwise, anisotropic nature is indicated. It is evident from Table 5 that both $B_{12}S$ and $B_{12}Se$ are slightly anisotropic.

The anisotropic nature of $B_{12}S$ and $B_{12}Se$ is further revealed by calculating the universal anisotropy index, A^U, using the relation[80] $A^U = 5\frac{G_V}{G_R} + \frac{B_V}{B_R} - 6 \geq 0$, where V and R denote the upper limit (Voigt, V) and lower limit (Reuss, R) of bulk and shear moduli. The obtained values of A^U also confirmed that both $B_{12}S$ and $B_{12}Se$ are mechanically anisotropic. From the listed values of anisotropy constants as presented in Table 5, it is seen that $B_{12}Se$ is more anisotropic than $B_{12}S$.

In the second part of this section, we have assessed the degree of anisotropy graphically for the Young's modulus, compressibility, shear modulus, and Poisson's ratio and summarized those in Table 6. The study is completed by plotting the Young's modulus, compressibility, shear modulus, and Poisson's ratio in 2D and 3D using the ELATE code.[81] The obtained 2D and 3D plots are presented in Figure 13a–d for $B_{12}S$. Plots for $B_{12}Se$ are qualitatively similar and are not shown. Figure 13a demonstrates the anisotropic nature of the Young's modulus (Y). As can be seen from the 2D plot, Y is isotropic in the xy plane but anisotropic in xz and yz planes. The maximum as well as minimum values are observed in the yz plane at different angles from the vertical or horizontal axis. The ratios between maximum and minimum values of Y are 1.69 and 3.22 for $B_{12}S$ and $B_{12}Se$, respectively, i.e., $B_{12}Se$ is significantly more anisotropic than $B_{12}S$ as far as the Young's modulus is concerned.

Figure 13b illustrates the anisotropic nature of compressibility (K), which is isotropic in the xy plane like Y. Both xz and yz planes exhibit similar anisotropic nature as well as degree in the anisotropy. For both the planes, the maximum of K lies on the vertical axis and minimum on the horizontal axis. The ratios between maximum and minimum values of K are 1.55 and 1.66 for $B_{12}S$ and $B_{12}Se$, respectively, i.e., $B_{12}Se$ is slightly more anisotropic than $B_{12}S$ for compressibility.

Figure 13c displays a complex anisotropy feature in the shear modulus (G), different from Y and K. The G is not isotropic in any plane but exhibits two values for each point of the planes. The blue color indicates the maximum values, while the red color indicates the minimum values. The maximum of G is obtained on the horizontal axis of both xy and xz planes for both the compounds. For the yz plane, the maximum of G lies at some angle above the positive horizontal axis as well as at some angle below the negative horizontal axis for $B_{12}S$. The maximum and minimum values of G lie almost midway of both horizontal and vertical axes in the yz plane for $B_{12}Se$. The ratios between maximum and minimum values of G are 1.79 and 3.70 for $B_{12}S$ and $B_{12}Se$, respectively, i.e., $B_{12}Se$ is significantly more anisotropic than $B_{12}S$ for G. The Poisson's ratio reveals a similar type of anisotropy to G, with two curves for each plane but much more complex than that of G. For this case, the

https://doi.org/10.1021/acsomega.1c05172
ACS Omega 2021, 6, 33899−33913

maximum and minimum values are also revealed by the outer and inner curves at each angle as shown in Figure 13d.

4. CONCLUSIONS

Density functional theory, incorporating different exchange−correlation functionals, is employed to characterize the structural, electronic band structure, and optical (dielectric function, refractive index, absorption coefficient, reflectivity, and loss function) properties of boron sub-sulfide ($B_{12}S$) and boron sub-selenide ($B_{12}Se$) compounds. Details of the mechanical properties such as different elastic moduli, Pugh's ratio, Poisson's ratio, various anisotropy parameters, fracture toughness, melting point, and machinability index have been estimated and discussed for the first time. The band gap is indirect in nature, and its value is exchange−correlation functional-sensitive. Large anisotropy in optical properties in the visible-light range to mid-UV is observed. The absorption coefficient for electric field polarization along the [100] direction of $B_{12}Se$ at the visible region is found to be 3.25×10^4 cm^{-1} that makes it competitive with renowned absorbance materials used in solar cell devices. The static value of the refractive index is comparable with some commercialized compounds such as corundum, silica glass, quartz, and soda lime glass. The lowest reflectivity spectrum starts with a value of 0.0742 (7.42%) for $B_{12}S$ and 0.0815 (8.15%) for the $B_{12}Se$ compound for the [001] polarization using the HSE06 functional. Such a pronounced absorption coefficient and a very low value of reflectivity spectra along with bulk optical anisotropy at the visible-light region are crucially important to design many optical devices such as LCD screens, screens for 3D movies, polarizers, wave plates, etc. Moreover, tunable band gaps of 2.27 and 1.30 eV for $B_{12}S$ and $B_{12}Se$, respectively, using the HSE06 functional in the visible-light region also augur well for solar cell device application although a thorough efficiency calculation is required. In view of the mechanical properties, the studied compounds have strongly anisotropic characteristics with a weak brittle nature confirmed from the shear to bulk modulus ratio and the Poisson's ratio. The calculated values of fracture toughness are 3.13 and 3.80 $MPam^{0.5}$, at least, for $B_{12}S$ and $B_{12}Se$, respectively, indicating high degrees of resistance to limit the propagation of the induced fracture in these two solids. The values of mechanical hardness using Miao's model are 31 and 24 GPa using the LDA functional for $B_{12}S$ and $B_{12}Se$, respectively, which are in reasonable agreement with experimental values. The origin of these high hardness values is successfully explained by considering the hybridization-dependent density of state values at the valence band near the Fermi level. Almost all the results disclosed in this work are novel in nature and should act as useful references for further investigations. We believe that our predicted results will inspire both experimentalists as well as theorists for further study of the physical properties of $B_{12}S$ and $B_{12}Se$ in the near future.

AUTHOR INFORMATION

Corresponding Authors

Md. Mukter Hossain − *Department of Physics, Chittagong University of Engineering and Technology (CUET), Chattogram 4349, Bangladesh;* orcid.org/0000-0003-2454-4996; Email: mukter_phy@cuet.ac.bd

Saleh Hasan Naqib − *Department of Physics, University of Rajshahi, Rajshahi 6205, Bangladesh*; Email: salehnaqib@yahoo.com

A. K. M. Azharul Islam − *Department of Physics, University of Rajshahi, Rajshahi 6205, Bangladesh; Department of Electrical and Electronic Engineering, International Islamic University Chittagong, Chittagong 4318, Bangladesh*; Email: azi46@ru.ac.bd

Authors

Md. Ashraf Ali − *Department of Physics, Chittagong University of Engineering and Technology (CUET), Chattogram 4349, Bangladesh*

Md. Mohi Uddin − *Department of Physics, Chittagong University of Engineering and Technology (CUET), Chattogram 4349, Bangladesh*

Complete contact information is available at: https://pubs.acs.org/10.1021/acsomega.1c05172

Notes

The authors declare no competing financial interest.

The datasets generated during the current study are available from the corresponding authors on a reasonable request.

ACKNOWLEDGMENTS

Authors are grateful to the Department of Physics, Chittagong University of Engineering & Technology (CUET), Chattogram 4349, Bangladesh, for providing the computing facilities for this work.

REFERENCES

(1) Cherednichenko, K. A.; Mukhanov, V. A.; Wang, Z.; Oganov, A. R.; Kalinko, A.; Dovgaliuk, I.; Solozhenko, V. L. Discovery of New Boron-Rich Chalcogenides: Orthorhombic B_6X (X=S, Se). *Sci. Rep.* **2020**, *10*, 9277.

(2) Cherednichenko, K. A.; Le Godec, Y.; Solozhenko, V. L. Equation of State of Boron Subarsenide $B_{12}As_2$ to 47 GPa. *High Pressure Res.* **2018**, *38*, 224−231.

(3) Emin, D. Icosahedral Boron-Rich Solids. *MRS Online Proc. Libr.* **1987**, *40*, 55.

(4) Xia, K.; Ma, M.; Liu, C.; Gao, H.; Chen, Q.; He, J.; Sun, J.; Wang, H.-T.; Tian, Y.; Xing, D. Superhard and Superconducting B_6C. *Mater. Today Phys.* **2017**, *3*, 76−84.

(5) Bolmgren, H.; Lundström, T. The Crystal Structure of a New Boron Selenide, $B_{12}Se_{2-x}B_x$. *J. Alloys Compd.* **1993**, *202*, 73−76.

(6) Hossain, M. M.; Ali, M. A.; Uddin, M. M.; Islam, A. K. M. A.; Naqib, S. H. Origin of High Hardness and Optoelectronic and Thermo-Physical Properties of Boron-Rich Compounds B_6X (X = S, Se): A Comprehensive Study via DFT Approach. *J. Appl. Phys.* **2021**, *129*, 175109.

(7) Cherednichenko, K. A.; Godec, Y. L.; Solozhenko, V. L. Equations of State of New Boron-Rich Selenides B_6Se and $B_{12}Se$. *arXiv:2106.04317 [cond-mat]* **2021**, 267.

(8) Cherednichenko, K. A.; Mukhanov, V. A.; Kalinko, A.; Solozhenko, V. L. High-Pressure Synthesis of Boron-Rich Chalcogenides $B_{12}S$ and $B_{12}Se$. *arXiv:2105.04450 [cond-mat]* **2021**, 162874.

(9) Lee, S.; Bylander, D. M.; Kleinman, L. Elastic Moduli of B_{12} and Its Compounds. *Phys. Rev. B* **1992**, *45*, 3245−3247.

(10) Enyashin, A. N.; Ivanovskii, A. L. Structural, Elastic, and Electronic Properties of Icosahedral Boron Subcarbides ($B_{12}C_3$, $B_{13}C_2$), Subnitride $B_{12}N_2$, and Suboxide $B_{12}O_2$ from Data of SCC-DFTB Calculations. *Phys. Solid State* **2011**, *53*, 1569.

(11) Wang, B.; Fan, Z.; Zhou, Q.; Xu, X.; Feng, M.; Cao, X.; Wang, Y. First Principles Calculations of the Vibrational Properties of Icosahedral Solid Boron Oxygen $B_{12}O_2$. *Phys. B* **2011**, *406*, 297−303.

(12) Korozlu, N.; Colakoglu, K.; Deligoz, E.; Aydin, S. The Elastic and Mechanical Properties of MB_{12} (M=Zr, Hf, Y, Lu) as a Function of Pressure. *J. Alloys Compd.* **2013**, *546*, 157−164.

(13) Pan, Y.; Jia, Y. First-Principles Study of Structure and Mechanical Properties of TMB_{12}(TM = W and Ti) Superhard Material under Pressure. *J. Mater. Res.* **2019**, *34*, 3554−3562.
(14) Sologub, O.; Matsushita, Y.; Mori, T. An α-Rhombohedral Boron-Related Compound with Sulfur: Synthesis, Structure and Thermoelectric Properties. *Scr. Mater.* **2013**, *68*, 289−292.
(15) Solozhenko, V. *Hardness of New Boron-Rich Chalcogenides $B_{12}S$ and $B_{12}Se$*. 2021, DOI: 10.33774/chemrxiv-2021-4pn07.
(16) Solozhenko, V. L. *Oxidation Resistance of Hard Boron-Rich Chalcogenides B_6X and $B_{12}X$ (X = S, Se)*. 2021, DOI: 10.33774/chemrxiv-2021-nxv20.
(17) Hohenberg, P.; Kohn, W. Inhomogeneous Electron Gas. *Phys. Rev.* **1964**, *136*, B864−B871.
(18) Perdew, J. P.; Burke, K.; Ernzerhof, M. Generalized Gradient Approximation Made Simple. *Phys. Rev. Lett.* **1996**, *77*, 3865−3868.
(19) Segall, M. D.; Lindan, P. J. D.; Probert, M. J.; Pickard, C. J.; Hasnip, P. J.; Clark, S. J.; Payne, M. C. First-Principles Simulation: Ideas, Illustrations and the CASTEP Code. *J. Phys.: Condens. Matter* **2002**, *14*, 2717−2744.
(20) Hossain, M. M.; Hossain, M. A.; Moon, S. A.; Ali, M. A.; Uddin, M. M.; Naqib, S. H.; Islam, A. K. M. A.; Nagao, M.; Watauchi, S.; Tanaka, I. $NaInX_2$ (X = S, Se) Layered Materials for Energy Harvesting Applications: First-Principles Insights into Optoelectronic and Thermoelectric Properties. *J. Mater. Sci.: Mater. Electron.* **2021**, *32*, 3878−3893.
(21) Ali, M. A.; Anwar Hossain, M.; Rayhan, M. A.; Hossain, M. M.; Uddin, M. M.; Roknuzzaman, M.; Ostrikov, K.; Islam, A. K. M. A.; Naqib, S. H. First-Principles Study of Elastic, Electronic, Optical and Thermoelectric Properties of Newly Synthesized $K_2Cu_2GeS_4$ Chalcogenide. *J. Alloys Compd.* **2019**, *781*, 37−46.
(22) Kohn, W.; Sham, L. J. Self-Consistent Equations Including Exchange and Correlation Effects. *Phys. Rev.* **1965**, *140*, A1133−A1138.
(23) Ehrenreich, H.; Cohen, M. H. Self-Consistent Field Approach to the Many-Electron Problem. *Phys. Rev.* **1959**, *115*, 786−790.
(24) Fischer, T. H.; Almlof, J. General Methods for Geometry and Wave Function Optimization. *J. Phys. Chem.* **1992**, *96*, 9768−9774.
(25) Monkhorst, H. J.; Pack, J. D. Special Points for Brillouin-Zone Integrations. *Phys. Rev. B* **1976**, *13*, 5188−5192.
(26) Park, S.; Lee, B.; Jeon, S. H.; Han, S. Hybrid Functional Study on Structural and Electronic Properties of Oxides. *Curr. Appl. Phys.* **2011**, *11*, S337−S340.
(27) Schira, R.; Latouche, C. DFT and Hybrid-DFT Calculations on the Electronic Properties of Vanadate Materials: Theory Meets Experiments. *New J. Chem.* **2020**, *44*, 11602−11607.
(28) Feng, J.; Xiao, B. Effective Masses and Electronic and Optical Properties of Nontoxic $MASnX_3$ (X = Cl, Br, and I) Perovskite Structures as Solar Cell Absorber: A Theoretical Study Using HSE06. *J. Phys. Chem. C* **2014**, *118*, 19655−19660.
(29) Clark, S. J.; Segall, M. D.; Pickard, C. J.; Hasnip, P. J.; Probert, M. I. J.; Refson, K.; Payne, M. C. First Principles Methods Using CASTEP. *Z. Kristallogr. Cryst. Mater.* **2005**, *220*, 567−570.
(30) Hadi, M. A.; Vovk, R. V.; Chroneos, A. Physical Properties of the Recently Discovered $Zr_2(Al_{1-x}Bi_x)C$ MAX Phases. *J. Mater. Sci.: Mater. Electron.* **2016**, *27*, 11925−11933.
(31) Matkovich, V. I. Interstitial Compounds of Boron. *J. Am. Chem. Soc.* **1961**, *83*, 1804−1806.
(32) Lundström, T. Structure and Bulk Modulus of High-Strength Boron Compounds. *J. Solid State Chem.* **1997**, *133*, 88−92.
(33) Gao, J.; Zeng, W.; Tang, B.; Zhong, M.; Liu, Q.-J. Optical, Electronic, and Mechanical Properties of p-Type Conductive Oxide $BaBiO_3$: A Density Functional Theory Study. *Chem. Phys. Lett.* **2020**, *761*, 138054.
(34) Green, M. A. Intrinsic Concentration, Effective Densities of States, and Effective Mass in Silicon. *J. Appl. Phys.* **1990**, *67*, 2944−2954.
(35) Wang, J.; Shu, H.; Zhao, T.; Liang, P.; Wang, N.; Cao, D.; Chen, X. Intriguing Electronic and Optical Properties of Two-Dimensional Janus Transition Metal Dichalcogenides. *Phys. Chem. Chem. Phys.* **2018**, *20*, 18571−18578.
(36) Benzie, P. W.; Elston, S. J. Optics of Liquid Crystals and Liquid Crystal Displays. In *Handbook of Visual Display Technology*; Chen, J., Cranton, W., Fihn, M., Eds.; Springer: Berlin, Heidelberg, 2012; pp. 1365−1385, DOI: 10.1007/978-3-540-79567-4_85.
(37) Penn, D. R. Wave-Number-Dependent Dielectric Function of Semiconductors. *Phys. Rev.* **1962**, *128*, 2093−2097.
(38) Liton, M. N. H.; Roknuzzaman, M.; Helal, M. A.; Kamruzzaman, M.; Islam, A. K. M. F. U.; Ostrikov, K.; Khan, M. K. R. Electronic, Mechanical, Optical and Photocatalytic Properties of Perovskite $RbSr_2Nb_3O_{10}$ Compound. *J. Alloys Compd.* **2021**, *867*, 159077.
(39) Tauc, J.; Menth, A. States in the Gap. *J. Non-Cryst. Solids* **1972**, *8-10*, 569−585.
(40) Makuła, P.; Pacia, M.; Macyk, W. How To Correctly Determine the Band Gap Energy of Modified Semiconductor Photocatalysts Based on UV−Vis Spectra. *J. Phys. Chem. Lett.* **2018**, *9*, 6814−6817.
(41) Roknuzzaman, M.; Hadi, M. A.; Ali, M. A.; Hossain, M. M.; Jahan, N.; Uddin, M. M.; Alarco, J. A.; Ostrikov, K. First Hafnium-Based MAX Phase in the 312 Family, Hf_3AlC_2: A First-Principles Study. *J. Alloys Compd.* **2017**, *727*, 616−626.
(42) Ali, M. S.; Islam, A. K. M. A.; Hossain, M. M.; Parvin, F. Phase Stability, Elastic, Electronic, Thermal and Optical Properties of $Ti_3Al_{1-x}SixC_2$ ($0 \leq x \leq 1$): First Principle Study. *Phys. B* **2012**, *407*, 4221−4228.
(43) Ali, M. A.; Hadi, M. A.; Hossain, M. M.; Naqib, S. H.; Islam, A. K. M. A. Theoretical Investigation of Structural, Elastic, and Electronic Properties of Ternary Boride MoAlB. *Phys. Status Solidi B* **2017**, *254*, 1700010.
(44) Ali, M. A.; Hossain, M. M.; Islam, A. K. M. A.; Naqib, S. H. Ternary Boride Hf_3PB_4: Insights into the Physical Properties of the Hardest Possible Boride MAX Phase. *J. Alloys Compd.* **2021**, *857*, 158264.
(45) Ali, M. A.; Hossain, M. M.; Uddin, M. M.; Hossain, M. A.; Islam, A. K. M. A.; Naqib, S. H. Physical Properties of New MAX Phase Borides M_2SB (M = Zr, Hf and Nb) in Comparison with Conventional MAX Phase Carbides M_2SC (M = Zr, Hf and Nb): Comprehensive Insights. *J. Mater. Res. Technol.* **2021**, *11*, 1000−1018.
(46) *Materials Science and Engineering: An Introduction*, 10th Edition | Wiley https://www.wiley.com/en-us/Materials+Science+and+Engineering%3A+An+Introduction%2C+10th+Edition-p-9781119405498 (accessed 2021−07 -29).
(47) Gencer, A. Electronic and Optical Properties of ASc_2S_4 (A = Ca, Sr) Compounds. *Phys. Scr.* **2021**, *96*, No. 075805.
(48) Jiang, C. First-Principles Study of Structural, Elastic, and Electronic Properties of Chromium Carbides. *Appl. Phys. Lett.* **2008**, *92*, No. 041909.
(49) Ali, M. A.; Naqib, S. H. Recently Synthesized $(Ti_{1-x}Mo_x)_2AlC$ ($0 \leq x \leq 0.20$) Solid Solutions: Deciphering the Structural, Electronic, Mechanical and Thermodynamic Properties via Ab Initio Simulations. *RSC Adv.* **2020**, *10*, 31535−31546.
(50) Masys, Š.; Jonauskas, V. A First-Principles Study of Structural and Elastic Properties of Bulk $SrRuO_3$. *J. Chem. Phys.* **2013**, *139*, 224705.
(51) Mouhat, F.; Coudert, F.-X. Necessary and Sufficient Elastic Stability Conditions in Various Crystal Systems. *Phys. Rev. B* **2014**, *90*, 224104.
(52) Voigt, W. *Lehrbuch der kristallphysik (mit ausschluss der kristalloptik)*; B.G. Teubner [J.W. Edwards: Leipzig; Berlin; [Ann Arbor, Mich., 1946.
(53) Reuss, A. Berechnung Der Fließgrenze von Mischkristallen Auf Grund Der Plastizitätsbedingung Für Einkristalle. *ZAMM - J. Appl. Math. Mech.* **1929**, *9*, 49−58.
(54) Hill, R. The Elastic Behaviour of a Crystalline Aggregate. *Proc. Phys. Soc. A* **1952**, *65*, 349−354.
(55) Ali, M. A.; Hossain, M. M.; Uddin, M. M.; Islam, A. K. M. A.; Jana, D.; Naqib, S. H. DFT Insights into New B-Containing 212 MAX Phases: Hf_2AB_2 (A = In, Sn). *J. Alloys Compd.* **2021**, *860*, 158408.

(56) Hossain, M. S.; Ali, M. A.; Hossain, M. M.; Uddin, M. M. Physical Properties of Predicted MAX Phase Borides Hf_2AB (A = Pb, Bi): A DFT Insight. *Mater. Today Phys.* **2021**, *27*, 102411.
(57) Ali, M. A.; Hossain, M. M.; Hossain, M. A.; Nasir, M. T.; Uddin, M. M.; Hasan, M. Z.; Islam, A. K. M. A.; Naqib, S. H. Recently Synthesized $(Zr_{1-X}Ti_x)_2AlC$ $(0 \leq x \leq 1)$ Solid Solutions: Theoretical Study of the Effects of M Mixing on Physical Properties. *J. Alloys Compd.* **2018**, *743*, 146−154.
(58) Rahaman, M. M.; Rubel, M. H. K.; Rashid, M. A.; Alam, M. A.; Hossain, K. M.; Hossain, M. I.; Khatun, A. A.; Hossain, M. M.; Islam, A. K. M. A.; Kojima, S.; Kumada, N. Mechanical, Electronic, Optical, and Thermodynamic Properties of Orthorhonmbic $LiCuBiO_4$ Crystal: A First−Priciples Study. *J. Mater. Res. Technol.* **2019**, *8*, 3783−3794.
(59) Barua, P.; Hossain, M. M.; Ali, M. A.; Uddin, M. M.; Naqib, S. H.; Islam, A. K. M. A. Effects of Transition Metals on Physical Properties of M_2BC (M = V, Nb, Mo and Ta): A DFT Calculation. *J. Alloys Compd.* **2019**, *770*, 523−534.
(60) Hossain, M. M.; Ali, M. A.; Uddin, M. M.; Hossain, M. A.; Rasadujjaman, M.; Naqib, S. H.; Nagao, M.; Watauchi, S.; Tanaka, I. Influence of Se Doping on Recently Synthesized $NaInS_{2-X}Se_x$ Solid Solutions for Potential Thermo-Mechanical Applications Studied via First-Principles Method. *Mater. Today Phys.* **2021**, *26*, 101988.
(61) Pugh, S. F. XCII. Relations between the elastic moduli and the plastic properties of polycrystalline pure metals. *London Edinburgh Philos. Mag. J. Sci.* **1954**, *45*, 823−843.
(62) Chen, X.-Q.; Niu, H.; Li, D.; Li, Y. Modeling Hardness of Polycrystalline Materials and Bulk Metallic Glasses. *Intermetallics* **2011**, *19*, 1275−1281.
(63) Miao, N.; Sa, B.; Zhou, J.; Sun, Z. Theoretical Investigation on the Transition-Metal Borides with Ta_3B_4-Type Structure: A Class of Hard and Refractory Materials. *Comput. Mater. Sci.* **2011**, *50*, 1559−1566.
(64) Mazhnik, E.; Oganov, A. R. A Model of Hardness and Fracture Toughness of Solids. *J. Appl. Phys.* **2019**, *126*, 125109.
(65) *USPEX Tools and Utilities — USPEX* https://uspex-team.org/en/uspex/tools (accessed 2021−07 -29).
(66) Jhi, S.-H.; Ihm, J.; Louie, S. G.; Cohen, M. L. Electronic Mechanism of Hardness Enhancement in Transition-Metal Carbonitrides. *Nature* **1999**, *399*, 132−134.
(67) Gao, F.; He, J.; Wu, E.; Liu, S.; Yu, D.; Li, D.; Zhang, S.; Tian, Y. Hardness of Covalent Crystals. *Phys. Rev. Lett.* **2003**, *91*, No. 015502.
(68) Ashby, M. F.; Cebon, D. Materials Selection in Mechanical Design. *J. Phys. IV France* **1993**, *03*, C7-1−C7-9.
(69) Ding, Z.; Zhou, S.; Zhao, Y. Hardness and Fracture Toughness of Brittle Materials: A Density Functional Theory Study. *Phys. Rev. B* **2004**, *70*, 184117.
(70) Niu, H.; Niu, S.; Oganov, A. R. Simple and Accurate Model of Fracture Toughness of Solids. *J. Appl. Phys.* **2019**, *125*, No. 065105.
(71) King, S. W.; Antonelli, G. A. Simple Bond Energy Approach for Non-Destructive Measurements of the Fracture Toughness of Brittle Materials. *Thin Solid Films* **2007**, *515*, 7232−7241.
(72) Haque, E. Outstanding Thermoelectric Performance of MCu_3X_4 (M = V, Nb, Ta; X = S, Se, Te) with Unaffected Band Degeneracy under Pressure. *ACS Appl. Energy Mater.* **2021**, *4*, 1942.
(73) Born, M. Thermodynamics of Crystals and Melting. *J. Chem. Phys.* **1939**, *7*, 591−603.
(74) Zhu, L.-F.; Grabowski, B.; Neugebauer, J. Efficient Approach to Compute Melting Properties Fully from Ab Initio with Application to Cu. *Phys. Rev. B* **2017**, *96*, 224202.
(75) Ledbetter, H.; Migliori, A. A General Elastic-Anisotropy Measure. *J. Appl. Phys.* **2006**, *100*, No. 063516.
(76) Tvergaard, V.; Hutchinson, J. W. Microcracking in Ceramics Induced by Thermal Expansion or Elastic Anisotropy. *J. Am. Ceram. Soc.* **1988**, *71*, 157−166.
(77) Lloveras, P.; Castán, T.; Porta, M.; Planes, A.; Saxena, A. Influence of Elastic Anisotropy on Structural Nanoscale Textures. *Phys. Rev. Lett.* **2008**, *100*, 165707.
(78) Ravindran, P.; Fast, L.; Korzhavyi, P. A.; Johansson, B.; Wills, J.; Eriksson, O. Density Functional Theory for Calculation of Elastic Properties of Orthorhombic Crystals: Application to $TiSi_2$. *J. Appl. Phys.* **1998**, *84*, 4891−4904.
(79) Chung, D. H.; Buessem, W. R. The Elastic Anisotropy of Crystals. *J. Appl. Phys.* **1967**, *38*, 2010−2012.
(80) Ranganathan, S. I.; Ostoja-Starzewski, M. Universal Elastic Anisotropy Index. *Phys. Rev. Lett.* **2008**, *101*, No. 055504.
(81) Gaillac, R.; Pullumbi, P.; Coudert, F.-X. ELATE: An Open-Source Online Application for Analysis and Visualization of Elastic Tensors. *J. Phys.: Condens. Matter* **2016**, *28*, 275201.

https://doi.org/10.1021/acsomega.1c05172
ACS Omega 2021, 6, 33899−33913